

# Design and Analysis of a GaN-Based Megahertz Integrated Motor Drive for a PCB Motor

Ozgur Gulsuna , Furkan Tokgoz , Furkan Karakaya , Ozan Keysan , Member, IEEE

**Abstract**—PCB motors present a compelling alternative to commercial electric motors due to their cost-effective mass production. Furthermore, integrated motor drives have gained popularity thanks to their high power density and ease of installation. However, PCB motors face challenges due to their large effective air gap and fewer turns, resulting in low phase inductance. This paper addresses these challenges by pairing the PCB motor with wide-bandgap devices and increasing the switching frequency to eliminate current ripple while reducing the size of filtering components, ultimately achieving a compact and efficient motor drive. The study explores various filtering options and decides upon for an L filter with line inductors on the motor phases. The losses of the system are analytically evaluated to a great extend leading to a selection of the switching frequency which is 1 MHz. Theoretical loss calculations are validated for both the electrical machine and inverter by means of calorimetric and electrical measurements. Finally, the integrated system is tested in motoring mode, operating at 5000 rpm and delivering 0.36 Nm of torque, resulting in an 82% efficiency. The paper concludes that increasing the switching frequency is a feasible solution for low inductance motor drives.

**Index Terms**—PCB motor, low inductance, integrated motor drive, wide-bandgap, GaN, loss distribution.

## I. INTRODUCTION

THE use of printed circuit boards (PCBs) instead of conventional wound electrical conductors in electromagnetic components has gained popularity over the years. Research into PCB-based magnetic components, including inductors, planar transformers, and coils for wireless power transfer, has attracted attention [1]–[4].

In terms of rotating machinery, axial-flux permanent magnet synchronous machines (AFPMMSMs) stand out to employ PCB stator technology [5], [6]. The pancake-like high-aspect-ratio composition of the AFPMMSMs contributes to compactness, torque density, and power density in the design [7]–[10]. Furthermore, the rigid composite structure of the circuit board serves a dual purpose by providing mechanical support for the stator windings [11].

Coreless printed stator designs are mainly explored in the literature due to their compatibility with existing automated

Manuscript received Month xx, 2xxx; revised Month xx, xxxx; accepted Month x, xxxx.

Ozgur Gulsuna and Ozan Keysan are with the Electrical and Electronics Engineering Department, Middle East Technical University, Ankara, 06800, Turkey.

Furkan Tokgoz is with the Department of Electronic and Electrical Engineering, University of Sheffield, S10 2TN, UK.

Furkan Karakaya is with the Electrical & Computer Engineering Department, University of Illinois Urbana-Champaign, Illinois, 61801, USA.

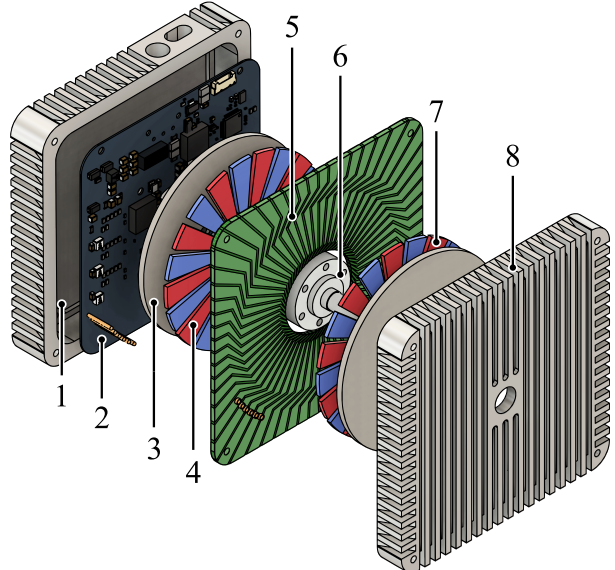


Fig. 1. Exploded view of the system. (1) Casing, (2) Motor drive board, (3) Rotor back-core, (4) Permanent magnets, (5) PCB stator, (6) Shaft, (7) Reciprocal magnets, (8) Casing cover.

manufacturing facilities, thus avoiding additional costs. As a result, in bulk orders the printed stators cost is just a fraction of other manufacturing technologies [12]. Lack of stator core reduces cogging torque and eliminates core losses on the stator. However, the trade-off is a larger effective air gap, leading to a low phase inductance [13]. This effect is elevated when comparing PCB stators to conventional copper windings, as printed boards generally have a fewer number of turns [7], [8]. An associated challenge in driving PCB AFPMMSMs is the emergence of large ripple currents due to the low phase inductance [14].

In the literature, various studies capturing the excitation of motors with low winding inductance are presented, all aiming to decrease the current ripple [14]–[21].

In [15], a small-scale ultrahigh-speed drive is developed for a motor with a phase inductance of  $6.2 \mu\text{H}$  and a rated power of 100 Watts. The discussion concerned with the selection of appropriate drive topology comparing voltage-source inverters (VSI) and current-source inverters (CSI), both fed by a dc-dc converter to regulate the dc link voltage to reduce ripple currents, rather than choosing a higher switching frequency.

Parallelly, a multilevel DC link inverter approach is discussed in [16]. The proposed inverter topology used string-connected semiconductors over the DC link to effectively

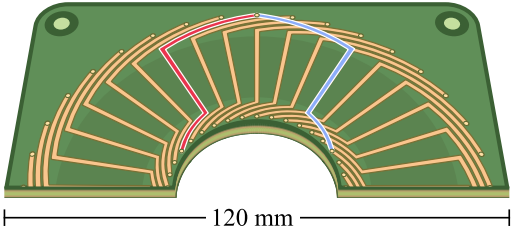


Fig. 2. Radial winding trace geometry of the PCB stator.

adjust the output voltage again to reduce the current ripple. A three-level neutral-point-clamped inverter is utilized in [14] along with block commutation to reduce the current ripple. In a high-speed drive scenario, a similar topology is implemented with sinusoidal current output incorporating neutral point balancing techniques, as described in [17].

Another approach to consider is the use of an output filter, which can take the form of a series inductor or an inductor-capacitor (LC) filter [18]–[21]. While this technique reduces the current ripple and attenuates electromagnetic emissions, it has certain drawbacks in terms of series voltage drop along with an increase in size, weight and losses due to the additional filtering components.

The coextending solution can be realized with emerging wide bandgap devices such as gallium nitride (GaN) transistors. These devices have low switching and conduction losses, enabling operation at high switching frequencies. Increasing the switching frequency to the megahertz (MHz) range facilitates a feasible design utilizing a three-phase inductor in series between the motor and the drive with a considerably small size [22], [23]. In robotics and aerospace applications, not only the electrical machine nor the proprietary converter power density is individually desired. In fact, the trend is to reduce the footprint as a whole to achieve a system-wise minimum volume [24]. Integrating the driver with the motor assembly in a single housing; hence the name integrated motor drive (IMD) has been applied to various systems with different power ratings [25]. For AFPMSMs, compactness is their advantage, which makes a low profile drive favourable.

In this paper, an integrated drive for an AFPMSM with a PCB stator is presented. The key contribution is the integration of a low-inductance motor drive with a PCB motor optimized for efficiency and torque density in a system-level dense design. A method to limit current ripple using increased switching frequency is proposed and tested. Furthermore, the power losses in the system are investigated in detail, contributing to the selection of an optimal switching frequency.

In section II, the permanent magnet (PM) machine is described, mechanical construction and design parameters are given. In Section III, a low-profile drive system capable of achieving switching frequencies up to 2 MHz is designed, angle sensing and control capabilities are discussed. Section IV is dedicated to a detailed analysis of losses and the integration of the motor with the drive. Experimental validation and performance criteria are addressed in section VI.

TABLE I  
SPECIFICATIONS OF THE PCB MOTOR.

<b>Rated speed</b>	6000 RPM	<b>Rated frequency</b>	1000 Hz
<b>Rated current</b>	4 A <sub>rms</sub>	<b>Rated torque</b>	0.36 Nm
<b>Phase resistance</b>	0.36 Ω	<b>Phase inductance</b>	3.1 μH
<b>Number of poles</b>	20	<b>Residual flux density</b>	1.38 T
<b>Height</b>	120 mm	<b>Width</b>	120 mm
<b>Axial length</b>	35 mm	<b>DC bus voltage</b>	48 V

## II. ELECTRICAL MACHINE DESCRIPTION

The electrical machine designed for this paper is an AFPMSM with PCB stator as illustrated in Fig. 1. The machine designed in double rotor single stator configuration which allows higher torque within a smaller volume at the expense of increased number of magnets [26], [27]. These magnets are affixed to the rotor cores while the stator has no ferromagnetic core, i.e. coreless or air cored. The absence of a stator core contributes to the elimination of core losses and reduction in the overall machine weight, thereby increases the efficiency. However, having no stator core also inherently leads to a low phase inductance. Moreover, the mechanical rigidity and manufacturing of the stator windings can be challenging problems to overcome as the stator is placed between two rotating bodies. PCB stators offer a viable solution with ease of production and affordability through PCB manufacturing capabilities. With the windings encased within FR-4 material, it solves two problems: mechanical rigidity and electrical insulation between copper traces. Moreover, the windings of the stator can be designed in any shape, angle, and length that can be used to optimize and improve the electrical performance of the machine. A few winding designs are investigated in detail in [28]. Radial winding topology offers better electrical performance with lower phase resistances compared to other winding types. So, radial winding with cooling traces is used in this paper, also depicted in Fig. 2.

Overall structure of the system with driver, housings, rotors, and the stator board is presented in Fig. 1. Specifications of the PM machine are provided in Table I, with a more detailed design discussion available in [29]. The driver is connected to the stator board via six pins. The system only requires two terminals for the DC supply and communication signals. The housings serve several purposes. The first is that they hold whole structure together and maintain the air gap. Secondly, the cooling of the stator and the driver is achieved using the large surface area of the housings. Lastly, housings act like an electromagnetic interference (EMI) shield.

## III. DESIGN OF THE INTEGRATED DRIVE SYSTEM

It is aimed to achieve precise control of both torque and speed while maintaining a high efficiency, all within a compact form factor. The proposed design operates with a voltage of 48 V, a common choice within the aerospace and automotive industries. Furthermore, it has the capability to provide the machine with an electrical power output of 230 W.

The main challenge faced by the electrical system is the low phase inductance, which results in a high current ripple issue. This study endeavors to address this problem by finding an

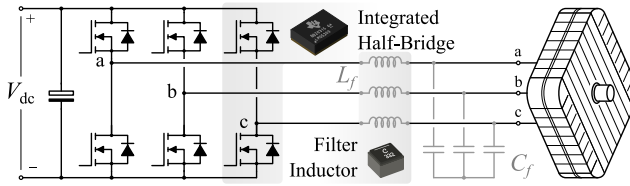


Fig. 3. Voltage-source-inverter topology consisting of half-bridge modules and filtering elements.

optimum switching frequency through the utilization of high-speed GaN devices.

#### A. Power Electronics Description

The power stage is designed with VSI topology as depicted in Fig. 3, comprised of half-bridge power modules, capable of functioning at frequencies of up to 10 MHz. These modules include integrated gate drivers and can manage up to 80 V while supplying 10 A<sub>rms</sub>, thanks to their low height and thermal resistance.

Several parallel multi-layer ceramic capacitors (MLCCs) are used in the DC link to reduce the height of the board. Increasing the switching frequency reduces the amount of capacitance, which allows the use of ceramic capacitors that have a longer lifespan. Hence, multiple parallel MLCCs are distributed across the DC link and at each half-bridge module, resulting in a combined capacitance of 100  $\mu$ F. However, it should be noted that achieving high dynamic control demands notably greater capacitance due to the stored energy in the rotor and mechanical load during transients.

The controller and power stage requires different voltage levels, therefore extra DC/DC converters are used. Due to the limited space available the controller and the power stage are not electrically isolated, therefore a careful layout design with separate voltage rails is needed to minimize undesired coupling between.

Potential EMI and overvoltage issues are tackled by limiting the distance between the motor and drive using a short connector. Moreover, unwanted radiation is mitigated through the utilization of filters at the DC input and motor interface. A common mode filter is employed at the input to reduce bearing currents, while the filter at the motor phases reduces the current harmonics, which will be discussed in the next section.

#### B. Output Filter Selection

An analysis capturing the expected current ripple is made. The aim is to investigate harmonic components in the output current that contribute to losses and efficiency reduction.

A switching function for three phase inverter in [30] is used to analytically calculate the current ripple for sinusoidal pulse-width modulation (SPWM), which is shown in (1).

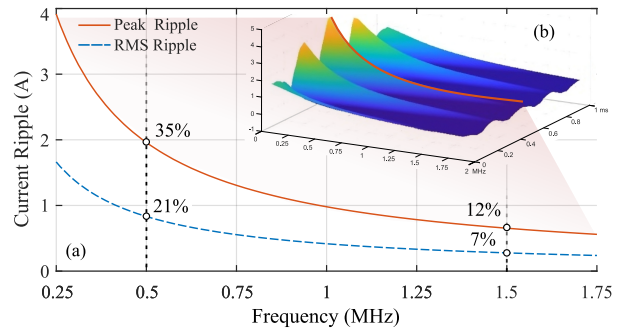


Fig. 4. (a) Expected reduction in current ripple as the switching frequency increases, without any filtering elements. (b) Current ripple change envelope in time domain for a single period.

Time varying switching function,  $S_a$ , depends on the modulation  $m_a$ , carrier frequency  $\omega_c$ , fundamental frequency  $\omega_o$ , and time.

The switching functions for all three phases are combined and multiplied by the DC link voltage in phasor domain, per phase, then divided by the motor impedance to formulate the current ripple.

Fig. 4 shows that for a range between 500 kHz and 1.5 MHz, the corresponding peak current ripple over the fundamental current's peak reduces from 35% to 12%. As for the root-mean-square (rms) of the current ripple, its ratio to the rms of the fundamental current lies between 21% and 7%. Due to the inverse relationship between frequency and ripple as shown in the figure, increasing the switching frequency is not feasible in reducing the output ripple further.

Filters can be used additionally to reduce the current harmonics. Among the passive filters can be employed, the L filter and the first-order LC filter are the most widely used. The L filter is utilized to increase the equivalent impedance seen by the high frequencies. However, the design restricts the inductor selection in low height and minimal loss criteria. Among the options that satisfy these criteria, the selected inductor comes with a height of 3.1mm and an inductance value of 3.3  $\mu$ H. This inductor employs a soft core material that curbs around 65% of the inductance at 8 A. Having an inductance that is equivalent to the winding inductance, a reduction in current ripple by 50% is expected for both the motor and the inverter.

LC filter is known to yield better differential mode filtering characteristics at the output, resulting in a sinusoidal current for the motor. However, implementing a filter with a cut-off frequency set to one-tenth of the switching frequency using the specified inductor, leads to a decrease in the overall impedance seen by the inverter due to the filter capacitor ( $C_f$ ). The resultant rise in the current ripple impacts the inverter, filter inductor and the filter capacitor, leading to an increase in losses over these components. To better visualize this effect, Fig. 5

$$S_a = \frac{1}{2} + \frac{m_a}{2} \cos(\omega_o t + \theta_o) + \frac{2}{\pi} \sum_{i=1}^{\infty} \left[ J_0(i \frac{\pi}{2} m_a) \sin(i \frac{\pi}{2}) \cos(i \omega_c t) \right] + \frac{2}{\pi} \sum_{i=1}^{\infty} \sum_{k=-\infty}^{\infty} \left[ \frac{\frac{1}{i} J_k(i \frac{\pi}{2} m_a) \sin(i \frac{\pi}{2} + k \frac{\pi}{2})}{\cos((i \omega_c t) + k(\omega_o t + \theta_o))} \right] \quad (1)$$

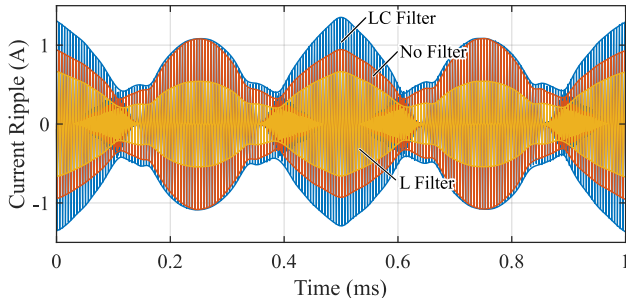


Fig. 5. Harmonics of the current ripple supplied by the inverter, excluding the fundamental frequency component, across different filter configurations, within a single fundamental period.

compares the current ripple among the various filter options in the time domain.

At the first glance, the implementation of an LC filter appears advantageous due to its effective reduction of current harmonics in motor windings. However, this approach necessitates a filter inductor ( $L_f$ ) with a higher inductance value and surface area to counterbalance the increased loss experienced in the filter and inverter. More preferred option is to employ an L filter, which permits a small current ripple to pass to the windings, yet this results in lesser current ripple over switches and filter inductors. Consequently, this approach reduces the size of the filter, enabling a more space-efficient design. Moreover, allowing the current ripple pass through the motor with least aggressive filter, the losses are shifted from the inverter to the windings where the heat is transferred with more ease.

### C. Controller & Peripherals Description

The control stage compromises the essential sensors and microcontroller required to generate the driving signals. As the level of integration increases, the number of peripherals and the control complexity also rise. This study aimed more complete integration, which includes a central microcontroller, two current sensors, an absolute angle sensor, temperature sensors, and isolated communication interfaces.

The main controller selected is the Texas Instruments TMS320F28375D, a 32-bit dual-core microcontroller operating at 200 MHz. The current sensors are of the hall effect type, with a frequency response that can filter high-frequency components. An absolute angle sensor is used in an off-axis configuration with an encoder magnet to further reduce the axial length. Temperature sensors with digital communication are employed to monitor the operating temperatures of the switches and controller. Lastly, the board has isolated communication interfaces, Universal Serial Bus (USB) and Controller Area Network (CAN).

### D. Printed Circuit Board Layout

The board layout is critical in enabling the various systems to work together within an integrated design. A four layer single board is designed to minimize the height, aiming to achieve a denser overall design.

The absolute angle sensor is located on the same plane where the shaft protrudes, near the center hole. The side-shaft configuration eliminates the need for an extra sensor

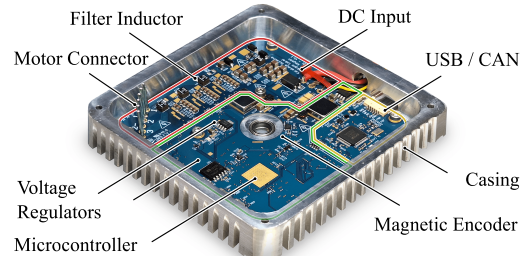


Fig. 6. Picture of the driver board mounted on motor case with various circuit blocks highlighted.

board. Current sensors are placed further to the side where the fringing flux of the permanent magnets can interfere with them, resulting in an angle-dependent periodic error. To address this issue, a look-up-table (LUT) method is used in conjunction with a calibration phase to compensate for the interference-caused errors. However, implementing this strategy necessitates the allocation of memory rather than computational expenses.

Fig. 6 lays out the power, control and communication stage boundaries with main components shown.

The board features multiple bolt holes to ensure good thermal contact between its components and the case. Additionally, thermal interface material (TIM) acts as a soft mechanic barrier for the fragile components. The primary sources of heat over the driver board are the switches, filters and the controller, with a total surface area of 335 mm<sup>2</sup> to the case. In contrast, the winding board has a total surface area of 668 mm<sup>2</sup> to the case, indicating a 20-fold lower thermal resistance to the case. In section IV, the distribution of the losses are examined in detail.

## IV. LOSS ESTIMATION & SWITCHING FREQUENCY SELECTION

Thermal design is one of the most challenging tasks in an integrated PCB motor, as compact designs often result in high loss densities. Therefore, a detailed loss analysis is crucial to ensure safe operation and identify factors that characterize the losses, such as switching frequency and current ripple.

The previous section gave an introduction about the relationship between frequency and current ripple, and subsequently, further estimations include this interconnection. The system's losses are categorized into two groups, namely electrical machine (EM) losses and inverter (INV) losses. The loss analysis calculation is formulated using analytical, experimental, and computational techniques. The contributions of these losses are compared, leading to a discussion on optimal switching frequency selection.

### A. Electrical Machine Losses

These losses are generated over the electrical machine part of the motor, exclusively over the windings. Conduction loss is calculated by the well known equation (2),

$$P_{EM(cond_f)} = 3I_{rms_f}^2 R_s \quad (2)$$

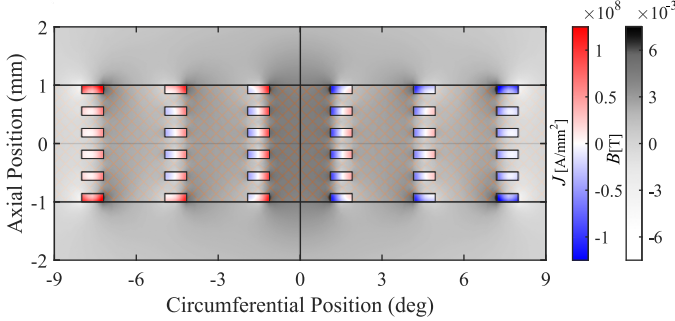


Fig. 7. 1-MHz FEM-simulated current density distribution and magnetic field intensity shown for PCB stator.

where  $I_{rms_f}$  is the fundamental current not considering harmonics.  $R_s$  is the measured phase resistance at  $47^\circ\text{C}$ , which stay relatively constant for frequencies under 100 kHz. However, high frequency harmonics due to ripple current result in extra power loss over the windings. Within the potential switching frequency range, this loss needs to be examined.

A 2D finite element model (FEM) is constructed capturing the machine geometry, shown in Fig. 7. The model is used to evaluate various losses of the electrical machine. The conduction loss per unit length of conductor is formulated in (3).

$$P_{EM(cond_h)} = \sum_{n=1}^3 \iint_S J_n^2(f_{sw}, I_n, n) \rho_{cu} dA \quad (3)$$

Here,  $n$  refers to the harmonic number expressed in orders of switching frequency, which is calculated for the first three components. The current density, denoted as  $J_n$ , over the conductor cross section area is influenced by several factors, including the skin effect, which is a result of the switching frequency and its harmonics and the proximity effect, related to current distribution. As the current distribution is contingent upon various factors and the interference of electric-magnetic fields, it is evaluated through finite-element analysis. The loss is estimated by integrating the current density over the conductor surface and multiplying it by the resistivity of copper ( $\rho_{cu}$ ) and the total conductor length.

In air cored machines, there are no stator core losses to consider. However, machines operating at high fundamental frequencies may still encounter eddy current losses within the stator windings.

Eddy current losses in stator can be described with (4).

$$P_{EM(eddy_s)} = \hat{B}_{PM}^2 f_0^2 \sigma_{cu} w_{cu}^2 V_{cu} \quad (4)$$

where  $\hat{B}_{PM}$  is the amplitude of the flux density,  $f_0$  is the fundamental frequency,  $\sigma_{cu}$  is the conductivity of copper and  $V_{cu}$  is the total copper volume exposed to the magnets.

$$P_{EM(eddy_r)} = \sum_{n=2}^4 \iint_S J_n^2(f_{sw}, I_n, n) \rho_{steel} dA \quad (5)$$

Eddy current losses also occur in the rotor core ( $P_{EM(eddy_r)}$ ) due to current harmonics. Although high-frequency harmonic

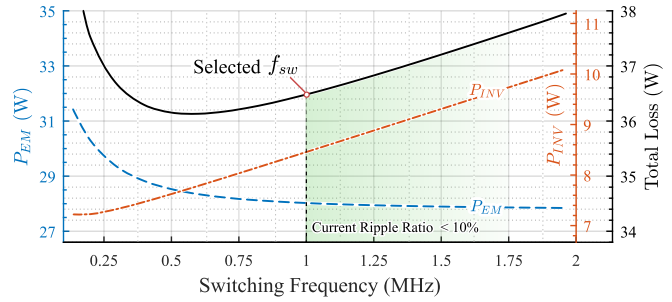


Fig. 8. Power loss trends of the inverter and electrical machine sections and the total loss curve of the system with respect to the switching frequency.

components induce an eddy current in the rotor, the magnetic field rotating at the fundamental frequency does not induce any current since the rotor rotates at the synchronous speed.

The final loss component on the electrical machine is the mechanical losses ( $P_{EM(mech)}$ ), which includes friction and windage losses. The method of calculation for these losses is experimental, and the procedure is explained in [29].

After analyzing losses in the frequency range from 100 kHz to 2 MHz, the general trend in electrical machine losses indicate a decrease as frequency increases, primarily due to the decrease in current ripple. In addition, the resemblance between the reduction patterns of current ripple and electrical machine losses implies that current ripple has a unnegelectable effect on the overall losses of the electrical machine.

### B. Inverter Losses

Inverter losses include the losses produced by the power stage, control stage, and peripherals. Conduction losses for a half-bridge module is given in (6), in which the current harmonics are taken into consideration.

$$P_{INV(cond)} = I_{rms_f}^2 R_{DS} + \sum_{n=1}^3 I_{rms(n)}^2 R_{DS} \quad (6)$$

Here,  $R_{ds}$  is the on resistance of the GaN switches and the harmonic components are calculated up to the third order.

Switching losses are calculated for a module with well known (7),

$$P_{INV(sw)} = V_{DC} I_{rms} \frac{(t_{rise} + t_{fall})}{2} f_{sw} \quad (7)$$

$V_{DC}$  stands for the DC bus voltage,  $t_{rise}$  and  $t_{fall}$  denote the rise and fall times of the switches at the rated current. Both  $t_{rise}$  and  $t_{fall}$  are approximately 2 nanoseconds, which considerably helps to reduce the switching losses.

GaN transistors do not have a body diode, however there is a similar effect observed for the third quadrant operation. This effect is modelled mathematically as,  $V_{SD}(\omega) = 0.45(I_{peak} \sin(\omega))^{0.39} + 1.55$  and used in the loss calculation with (8).

$$P_{INV(third)} = \int_0^{\pi/2} \frac{V_{SD}(\omega) I_{peak} \sin(\omega) t_{dead} f_{sw}}{\pi/2} d\omega \quad (8)$$

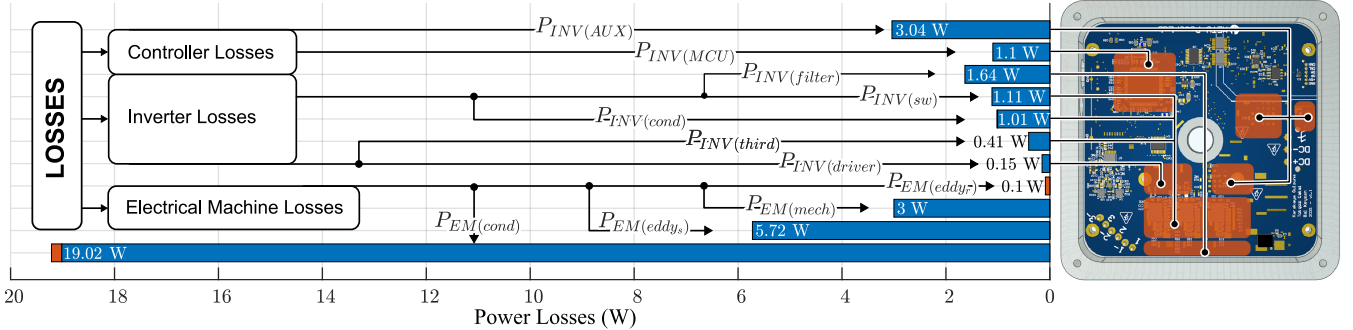


Fig. 9. Bar-tree combined graph for power losses in the system at the rated speed with 1 MHz switching frequency.

The switching device results in higher losses for longer dead-time durations ( $t_{dead}$ ). The duration, considering the frequency range and rise-fall times, is selected as 8 nanoseconds.

Driver losses are energy lost in charging and discharging the gate of the semiconductor devices in each cycle. Since the switching frequency is expected to be high, this loss is also calculated with the equation provided in (9).

$$P_{INV(driver)} = V_{gs} I_{dd} \quad (9)$$

Here,  $I_{dd}$  is the gate driver current which increases linearly with the switching frequency as indicated in the datasheet.

Filter inductors' contribution to the loss generation is particularly important because there is no direct heat path between the inductors and the case. The conduction loss over the inductors is given in 10.

$$P_{INV(filter)} = I_{rms}^2 R_{ind} + P_{core} \quad (10)$$

Lastly, the power consumption of the microcontroller and auxiliary converters, namely  $P_{MCU}$  and  $P_{AUX}$  are found experimentally.

Inverter losses exhibit a linear increase with an increasing switching frequency for the same range. Conversely, losses of electrical machines follow an opposite trend, indicating the existence of a minimum point in-between. Despite this point, greater attention should be paid to the inverter side since it has smaller total contact with the case.

### C. Switching Frequency Selection

The appropriate switching frequency is determined by several factors, including current ripple limit, minimizing losses, and operating temperature limits.

The total power loss and operation limits are depicted in Fig. 8. A ripple ratio limit of 10% is imposed, which limits the minimum switching frequency to 1 MHz. The thermal limit is correlated with the loss distribution, especially for the inverter side. The intersection of these limits yields the convenient range of switching frequencies.

From an efficiency standpoint, minimizing total losses is preferable. For the designed machine, total losses reach a minimum point at around 600 kHz, but the maximum deviation in total loss, within the frequency range analyzed is only 8%. This difference translates to a maximum power loss difference

of approximately 2 W, with a corresponding efficiency impact of below 1%.

Increasing the switching frequency further reduces the current harmonics, enhance controllability, and lower computational load. However, increasing the frequency further may not be as effective due to the inverse relationship between frequency and ripple current.

Higher switching frequencies also increase the thermal burden on the inverter because of the increased switching losses. Furthermore the small contact area with the case means that even slight increments in losses have an impact on the junction temperatures of the GaN switches.

A switching frequency of 1 MHz is chosen, despite not being the most efficient point of operation for the overall system, to set a balance point between the current ripple and temperature of the inverter board.

Having losses laid out and variables such as switching frequency determined involves taking steps towards a loss distribution analysis, which is particularly important in an integrated system. The loss distribution of the machine is constructed for a switching frequency of 1 MHz.

The Fig. 9 displays a bar-tree combined graph illustrating the losses and respective components. Blue bars represent losses due to the fundamental component, while orange bars represent losses resulted from current harmonics.

The losses on the motor side are dominated by conduction and eddy current losses. The optimal trace width selection heavily depends on these two losses, as it helps to minimize the machine related losses to a great extent. Analysis of the losses indicates that the eddy current losses on the stator are quite noticeable, even with no stator core. Another notice is that, at a switching frequency of 1 MHz, the total harmonic losses only account for 0.75% of the machine losses. However, for 200 kHz the percentage is 7.5%. This suggests that for integrated drives with increased switching frequencies and non-zero current ripple, low-inductance drive design becomes more feasible.

## V. EXPERIMENTAL VERIFICATION

A prototype is constructed to verify the design and analysis, assessing the effectiveness of design procedures, including analytical modeling, finite-element simulations, and control

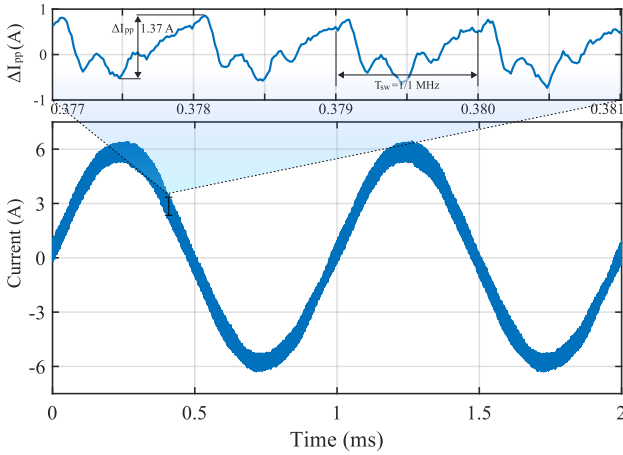


Fig. 10. Current ripple measurement using RL load with matched impedance.

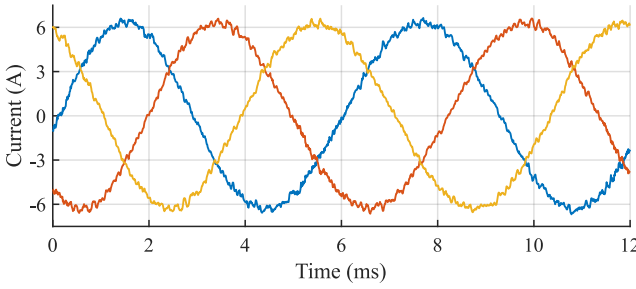


Fig. 11. Phase currents of the motor captured with integrated drive system at the rated torque and 1000 rpm.

methodologies. The corresponding experimental setup shown in Fig. 12 is built to validate the design and the analysis.

First, the inverter board is tested with a resistive-inductive (RL) load that matches the rated load conditions. Particularly, the inductance is matched of the assembled stator's and the voltage drop over the resistance is close to the machine's back-emf voltage at rated speed. As a consequence the operating conditions such as modulation index and phase current are set similar to the ones at the motoring mode of operation. The current waveform observed in this experiment for the rated conditions can be seen in Fig. 10.

The current ripple value observed in RL load case closely matched the analysis at 1 MHz switching frequency. The maximum peak-to-peak and rms current ripple values and corresponding percentages are given in Table II. This experiment provided a verification for the output filter, creating a smooth control setting with low current harmonics.

Using a calorimeter setup, a 9 W of power loss is measured to be dissipated over the driver at rated conditions with RL load. The analytic counterpart for the driver part estimated about 8.5 W from the bar-tree graph, which shows that they are in good agreement.

Secondly, machine side losses at generator mode are measured, which do not include the losses due to the current ripple. The result came out to be 32 W with electrical measurement when compared with the analytical 26.4 W counterpart including the harmonics.

In the motoring mode, field-oriented-control with SPWM is used to drive the motor at 5000 rpm with 1 MHz switch-

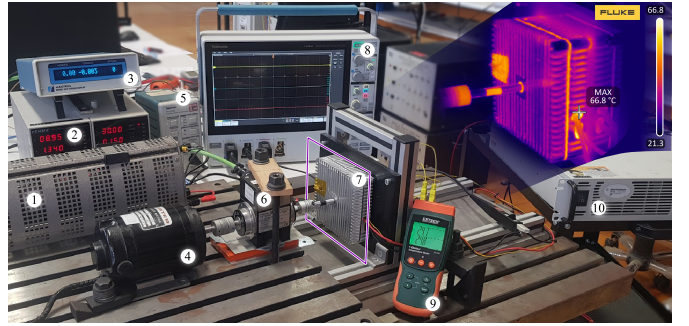


Fig. 12. Experimental setup for the motoring tests with the thermal camera view, under rated load. (1) Resistive load for the DC generator, (2) Field supply for the DC generator, (3) Torque display, (4) DC generator, (5) High bandwidth current probe, (6) Torque sensor, (7) Prototype under test, (8) Oscilloscope, (9) Temperature logger, (10) DC supply.

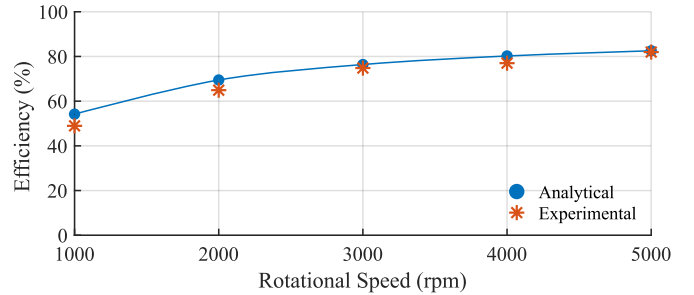


Fig. 13. Efficiency plot of the whole system with respect to the rotational speed at full load torque.

ing frequency. Within the controller, current measurement is updated at every 100 kHz, and speed measurement at 1 kHz. A feed-forward compensator is implemented to increase the controller stability at high rotational speeds.

The system is tested at different mechanical loadings, the full load case resulted in 82% efficiency at 5000 rpm, 0.36 Nm. Analytic model yielding at 83.5% and hence the model and the experimental result are cooperating. An efficiency plot capturing all tested operation points is given in Fig. 13.

## VI. CONCLUSION

In this paper, an integrated motor drive system is designed and implemented for a low inductance axial-flux permanent magnet motor with a PCB stator, employing GaNFETs for high-frequency operation. The selection of filter is based on efficiency and size constraints, primarily focusing on limiting current ripple subjected to the switches. The distribution of the loss components within a feasible switching frequency range is discussed, with inverter losses accounting for one-third of the electrical machine losses, with a remark on the inverter having a smaller surface area. A switching frequency of 1 MHz is chosen, taking into account filter selection,

TABLE II  
RMS AND PEAK-TO-PEAK VALUES OF THE CURRENT RIPPLE.

	$I_{RMS}$	%	$I_{pp}$	%
Analytical	0.25 $A_{rms}$	6.38%	1.32 $A_{pp}$	10.45%
Experimental	0.33 $A_{rms}$	7.98%	1.50 $A_{pp}$	11.73%

losses, and distribution, resulting in a reduction of harmonic components' contribution. Experimental results for both the electrical machine and inverter align well with the analytical loss model, demonstrating its suitability for evaluating high-frequency harmonic components of losses. The integrated system is successfully tested at 5000 rpm and 0.36 Nm with a 1 MHz switching frequency, affirming the viability of this approach in limiting current ripple in low inductance motor drive scenario.

## REFERENCES

- [1] A. Olivei, "Optimized miniature thin-film planar inductors, compatible with integrated circuits," *IEEE Transactions on Parts, Materials and Packaging*, vol. 5, DOI 10.1109/TPMP.1969.1136062, no. 2, pp. 71–88, 1969.
- [2] C. Marxgut, J. Muhlethaler, F. Krismer, and J. W. Kolar, "Multiobjective optimization of ultraflat magnetic components with pcb-integrated core," *IEEE Transactions on Power Electronics*, vol. 28, DOI 10.1109/TPEL.2012.2226917, no. 7, pp. 3591–3602, 2013.
- [3] S. Raju, R. Wu, M. Chan, and C. P. Yue, "Modeling of mutual coupling between planar inductors in wireless power applications," *IEEE Transactions on Power Electronics*, vol. 29, DOI 10.1109/TPEL.2013.2253334, no. 1, pp. 481–490, 2014.
- [4] B. Li, Q. Li, and F. C. Lee, "High-frequency pcb winding transformer with integrated inductors for a bi-directional resonant converter," *IEEE Transactions on Power Electronics*, vol. 34, DOI 10.1109/TPEL.2018.2874806, no. 7, pp. 6123–6135, 2019.
- [5] M.-C. Tsai and L.-Y. Hsu, "Design of a miniature axial-flux spindle motor with rhomboidal pcb winding," *IEEE Transactions on Magnetics*, vol. 42, DOI 10.1109/TMAG.2006.879438, no. 10, pp. 3488–3490, 2006.
- [6] G.-J. Yan, L.-Y. Hsu, J.-H. Wang, M.-C. Tsai, and X.-Y. Wu, "Axial-flux permanent magnet brushless motor for slim vortex pumps," *IEEE Transactions on Magnetics*, vol. 45, DOI 10.1109/TMAG.2009.2022499, no. 10, pp. 4732–4735, 2009.
- [7] S. Paul, M. Farshadnia, A. Pouramin, J. Fletcher, and J. Chang, "Comparative analysis of wave winding topologies and performance characteristics in ultra-thin printed circuit board axial-flux permanent magnet machine," *IET Electric Power Applications*, vol. 13, DOI https://doi.org/10.1049/iet-epa.2018.5417, no. 5, pp. 694–701, 2019.
- [8] N. S., S. P. Nikam, S. Pal, A. K. Wankhede, and B. G. Fernandes, "Performance comparison between pcb-stator and laminated-core-stator-based designs of axial flux permanent magnet motors for high-speed low-power applications," *IEEE Transactions on Industrial Electronics*, vol. 67, DOI 10.1109/TIE.2019.2931503, no. 7, pp. 5269–5277, 2020.
- [9] J. Zhao, T. Ma, X. Liu, G. Zhao, and N. Dong, "Performance analysis of a coreless axial-flux pmsm by an improved magnetic equivalent circuit model," *IEEE Transactions on Energy Conversion*, vol. 36, DOI 10.1109/TEC.2020.3040009, no. 3, pp. 2120–2130, 2021.
- [10] J. Zhao, Y. Wang, T. Ma, X. Liu, and J. Li, "Losses and thermal analysis of an integrated pcb coreless axial flux pmsm with the drive system," *IEEE Transactions on Industrial Electronics*, vol. 70, DOI 10.1109/TIE.2022.3229395, no. 11, pp. 11022–11032, 2023.
- [11] R. Knippel, M. Tisler, and D. C. Ludois, "Printed circuit board structural properties and spiral groove trace conductors for hydrodynamic gap maintenance in axial flux rotating machines," in *2019 IEEE Energy Conversion Congress and Exposition (ECCE)*, DOI 10.1109/ECCE.2019.8913303, pp. 6084–6091, 2019.
- [12] F. Tokgoz, "Analytical modelling and multi-objective optimization of axial-flux permanent magnet machine with various pcb stators and development of a gan switched integrated motor drive pcb motor," Master's thesis, Middle East Technical University, 2022.
- [13] N. S., S. P. Nikam, S. Singh, S. Pal, A. K. Wankhede, and B. G. Fernandes, "High-speed coreless axial-flux permanent-magnet motor with printed circuit board winding," *IEEE Transactions on Industry Applications*, vol. 55, DOI 10.1109/TIA.2018.2872155, no. 2, pp. 1954–1962, 2019.
- [14] S. De, M. Rajne, S. Poosapati, C. Patel, and K. Gopakumar, "Low-inductance axial flux bldc motor drive for more electric aircraft," *IET Power Electronics*, vol. 5, DOI 10.1049/iet-pel.2010.0329, p. 124, 2012. [Online]. Available: <http://digital-library.theiet.org/content/journals/10.1049/iet-pel.2010.0329>
- [15] C. Zwyssig, S. D. Round, and J. W. Kolar, "An ultrahigh-speed, low power electrical drive system," *IEEE Transactions on Industrial Electronics*, vol. 55, DOI 10.1109/TIE.2007.911950, no. 2, pp. 577–585, 2008.
- [16] G.-J. Su and D. Adams, "Multilevel dc link inverter for brushless permanent magnet motors with very low inductance," in *Conference Record of the 2001 IEEE Industry Applications Conference. 36th IAS Annual Meeting (Cat. No.01CH37248)*, vol. 2, DOI 10.1109/IAS.2001.955549, pp. 829–834 vol.2, 2001.
- [17] C. Li, T. Yang, P. Kulsangcharoen, G. L. Calzo, S. Bozhko, C. Gerada, and P. Wheeler, "A modified neutral point balancing space vector modulation for three-level neutral point clamped converters in high-speed drives," *IEEE Transactions on Industrial Electronics*, vol. 66, DOI 10.1109/TIE.2018.2835372, no. 2, pp. 910–921, 2019.
- [18] J. Steinke, "Use of an lc filter to achieve a motor-friendly performance of the pwm voltage source inverter," *IEEE Transactions on Energy Conversion*, vol. 14, DOI 10.1109/60.790930, no. 3, pp. 649–654, 1999.
- [19] J. Salomaki, M. Hinkkanen, and J. Luomi, "Influence of inverter output filter on maximum torque and speed of pmsm drives," in *2007 Power Conversion Conference - Nagoya*, DOI 10.1109/PCCON.2007.373066, pp. 852–859, 2007.
- [20] P. Mishra and R. Maheshwari, "Design, analysis, and impacts of sinusoidal lc filter on pulsewidth modulated inverter fed-induction motor drive," *IEEE Transactions on Industrial Electronics*, vol. 67, DOI 10.1109/TIE.2019.2913824, no. 4, pp. 2678–2688, 2020.
- [21] W. Geng, Z. Zhang, and Q. Li, "Analysis and experimental verification of a conventional inverter with output lc filter to drive ironless stator axial-flux pm motor," *IEEE Transactions on Transportation Electrification*, vol. 7, DOI 10.1109/TTE.2021.3062090, no. 4, pp. 2600–2610, 2021.
- [22] A. K. Morya, M. C. Gardner, B. Anvari, L. Liu, A. G. Yepes, J. Doval-Gandoy, and H. A. Toliat, "Wide bandgap devices in ac electric drives: Opportunities and challenges," *IEEE Transactions on Transportation Electrification*, vol. 5, DOI 10.1109/TTE.2019.2892807, no. 1, pp. 3–20, 2019.
- [23] N. He, M. Chen, J. Wu, N. Zhu, and D. Xu, "20-kw zero-voltage-switching sic-mosfet grid inverter with 300 khz switching frequency," *IEEE Transactions on Power Electronics*, vol. 34, DOI 10.1109/TPEL.2018.2866824, no. 6, pp. 5175–5190, 2019.
- [24] S. Wu, C. Tian, W. Zhao, J. Zhou, and X. Zhang, "Design and analysis of an integrated modular motor drive for more electric aircraft," *IEEE Transactions on Transportation Electrification*, vol. 6, DOI 10.1109/TTE.2020.2992901, no. 4, pp. 1412–1420, 2020.
- [25] J. Wang, Y. Li, and Y. Han, "Integrated modular motor drive design with gan power fets," *IEEE Transactions on Industry Applications*, vol. 51, DOI 10.1109/TIA.2015.2413380, no. 4, pp. 3198–3207, 2015.
- [26] A. Cavagnino, M. Lazzari, F. Profumo, and A. Tenconi, "A comparison between the axial flux and the radial flux structures for pm synchronous motors," in *Conference Record of the 2001 IEEE Industry Applications Conference. 36th IAS Annual Meeting (Cat. No.01CH37248)*, vol. 3, DOI 10.1109/IAS.2001.955750, pp. 1611–1618 vol.3, 2001.
- [27] S. Huang, J. Luo, F. Leonardi, and T. Lipo, "A comparison of power density for axial flux machines based on general purpose sizing equations," *IEEE Transactions on Energy Conversion*, vol. 14, DOI 10.1109/60.766982, no. 2, pp. 185–192, 1999.
- [28] F. Tokgoz, G. Cakal, and O. Keysan, "Comparison of pcb winding topologies for axialflux permanent magnet synchronous machines," *IET Electric Power Applications*, vol. 14, DOI 10.1049/iet-epa.2020.0622, no. 13, p. 2577, 2020.
- [29] F. Tokgoz, O. Gulsuna, F. Karakaya, G. Cakal, and O. Keysan, "Mechanical and thermal design of an optimized pcb motor for an integrated motor drive system with ganfets," *IEEE Transactions on Energy Conversion*, vol. 38, DOI 10.1109/TEC.2022.3213896, no. 1, pp. 653–661, 2023.
- [30] B. B. S.R. Bowes, "Novel approach to the analysis and synthesis of modulation processes in power convertors," *Proceedings of the Institution of Electrical Engineers*, vol. 122, pp. 507–513(6), May. 1975.



**Ozgur Gulsuna** received the B.Sc. degree in Electrical-Electronics Engineering from Middle East Technical University (METU), Ankara, Turkey, in 2023. Currently pursuing his M.Sc. degree in the same department.

Current research interests capture data driven design, reliability and durability in power electronics and wide bandgap devices.



**Furkan Karakaya** (Student Member, IEEE) received the B.Eng. and M.Sc. degrees in electrical and electronics engineering from Middle East Technical University, Ankara, Turkey, in 2017 and 2020, respectively.

He is currently pursuing the Ph.D. degree with University of Illinois Urbana-Champaign as a member of the Power Energy Systems Research Group. His current research interests include power electronics, device characterization, applications and reliability of wide bandgap transistors, and integrated and fault-tolerant electrical motor drivers.



**Furkan Tokgoz** (Student Member, IEEE) received the B.Sc. and M.Sc. degrees in Electrical-Electronics Engineering from Middle East Technical University, Ankara, Turkey, in 2019 and 2022, respectively. He is currently pursuing his Ph.D. in the University of Sheffield, UK as a member of Electrical Machines and Drives (EMD) group.

His current research interests are less rare-earth permanent magnet machines for electric vehicles, integrated motor drive axial-flux machines, and PCB stators.



**Ozan Keysan** (Member, IEEE) received the B.Sc. and M.Sc. degrees from Middle East Technical University (METU), Ankara, Turkey in 2005 and 2008, respectively, and the Ph.D. degree from the University of Edinburgh, Edinburgh, U.K., in 2014.

He is currently an Assistant Professor with the Department of Electrical and Electronics Engineering, METU. His current research interests include renewable energy, design and optimization of electrical machines, smart grids, superconducting machines, and permanent-magnet machines.